

Anisotropic energy transfers in quasi-static magnetohydrodynamic turbulence

K. Sandeep Reddy,^{1, a)} Raghendra Kumar,^{2, b)} and Mahendra K. Verma^{3, c)}

¹⁾*Department of Mechanical Engineering, Indian Institute of Technology, Kanpur 208016, India*

²⁾*Theoretical Physics Division, Bhabha Atomic Research Centre, Mumbai 400 085, India*

³⁾*Department of Physics, Indian Institute of Technology, Kanpur 208016, India*

(Dated: 3 December 2024)

We perform direct numerical simulations of quasi-static magnetohydrodynamic turbulence, and compute various energy transfers including ring-to-ring and conical energy transfers, and energy fluxes of the perpendicular and parallel components of the velocity field. We show that the rings with higher polar angles transfer energy to ones with lower polar angles. For large interaction parameters, the dominant energy transfer takes place near the equator (polar angle $\theta \approx \frac{\pi}{2}$). The energy transfers are local both in wavenumbers and angles. The energy flux of the perpendicular component is from higher to lower wavenumbers (inverse), while that of the parallel component is from lower to higher wavenumbers (forward). Our results are consistent with earlier results that indicate two-dimensional three-component (2D3C) nature of quasi-static magnetohydrodynamic (MHD) flows.

I. INTRODUCTION

Liquid metal flows under strong magnetic field occur in geophysics, metallurgical applications like metal-plate rolling, heat exchangers of the proposed fusion reactor ITER, etc. These flows are described by magnetohydrodynamics (MHD), which involves equations for the velocity and magnetic fields. Liquid metals have small magnetic Prandtl numbers Pm , which is a ratio of the kinematic viscosity ν and magnetic diffusivity η .^{1,2}

The flow velocity in a typical industrial application is rather small. Hence the magnetic Reynolds number Rm (UL/η , where U and L are the large-scale velocity and length scales respectively) for such flows is quite small. A limiting case of such flows, called the quasi-static limit^{1,2} ($Rm \rightarrow 0$), provides further simplification; here the time derivative of the magnetic field is negligible compared to the magnetic diffusion term. Experiments^{3,4} and numerical simulations⁵⁻⁷ show that the flow becomes quasi two-dimensional when subjected to a strong mean magnetic field. In the present paper, we will discuss the energy transfers in the quasi-static MHD. We will highlight the energy transfers responsible for making the flow quasi two-dimensional.

Experimental studies by Alemany *et al.*,³ and Kolesnikov and Tsinober⁴ showed that the kinetic energy spectrum scales with wavenumber k as k^{-3} . They ascribe this scaling to the two-dimensionalization of the flow. The experiments performed by Branover *et al.*⁸ on mercury under external magnetic field exhibit energy spectrum as $k^{-\alpha}$ with $\alpha \in \{-11/3, -7/3, -5/3\}$. For liquid sodium experiments in a channel, Eckert *et al.*,⁹ reported a steepening of the energy spectrum when the

external magnetic field is increased.

The external magnetic field makes the flow anisotropic. For strong magnetic field, Moffatt¹⁰ predicted a rapid decay of isotropic three dimensional turbulence to a two-dimensional state. Schumann⁵ studied decaying homogeneous quasi-static MHD using numerical simulations and verified Moffatt's predictions.¹⁰ Zikanov and Thess⁶ showed that for moderate interaction parameters, the turbulence remains quasi two-dimensional for several eddy turnover times before it is interrupted by strong bursts of three dimensional turbulence. Burattini *et al.*^{11,12} addressed the issue of anisotropy in quasi static MHD turbulence. They computed the kinetic energy spectrum and showed how the anisotropy varies with respect to the direction of the external magnetic field.

For strong applied magnetic field, using direct numerical simulations (DNS) and eddy-damped quasi-normal Markovian (EDQNM) model, Favier *et al.*^{7,13} showed that in a quasi two-dimensional state, the toroidal component of velocity field has more energy compared to the poloidal component of the velocity. This is termed as two-dimensional three-components (2D3C) flow,¹⁴ unlike two-dimensional flow with only two components. Favier *et al.*⁷ attribute the quasi two-dimensional nature of the flow to the Joule dissipation occurring at short-time scales, and to the anisotropy of the flow due to the external magnetic field. Reddy and Verma¹⁵ studied energy spectrum for very large magnetic field, and observed an exponential spectrum. They also computed anisotropic energy spectrum using ring decomposition, and showed that the energy is concentrated near the equator, a result consistent with those of Favier *et al.*,⁷ Burattini *et al.*,¹¹ and Poth erat and Dymkou.¹⁶ In the present paper we compute the ring-to-ring and conical energy transfers, as well as energy fluxes of the parallel and perpendicular components of the velocity field. These studies also reveal dominant energy transfers near the equator, as well as an inverse cascade for the perpendicular component of the velocity field, and a forward cascade for the parallel

^{a)}Electronic mail: ksreddy@iitk.ac.in

^{b)}Electronic mail: raghav@barc.gov.in

^{c)}Electronic mail: mkv@iitk.ac.in

component.

Boeck *et al.*¹⁷ performed DNS of liquid metal flow in a channel, in which they observed sudden three-dimensional bursts in a steady two-dimensional flow. In the presence of no-slip walls, a departure from quasi two-dimensional to a three-dimensional behavior is observed in the flow field.^{18–20} Note that the flow structures with no-slip walls are quite different from those with periodic domains. Yet, periodic box computations provide interesting insights into the bulk flow.

The energy spectrum of liquid metal flows has been studied by a large number of scientists and engineers (see above). However, diagnostics like energy flux, shell-to-shell energy transfer, etc., are much less studied in this field. In fluid turbulence, the turbulence is homogeneous and isotropic in the inertial range.²¹ Also, in the inertial range, Kolmogorov’s flux is constant, and the shell-to-shell energy transfer is forward and local (maximum transfers between the neighboring shell).²¹ However, in liquid metal flows, the mean magnetic field induces anisotropic energy transfers, which are quantified using angular-dependent energy flux and ring-to-ring transfers. We use the formalism proposed by Dar *et al.*,²² Verma,²³ and Teaca *et al.*²⁴ to compute these quantities.

For magnetohydrodynamic flows with unit magnetic Prandtl number, Teaca *et al.*²⁴ computed the energy transfers among the spectral rings (see Fig. 1). These rings are specified by their radii and sector indices (see Fig. 2). For convenience, we refer to the rings near the pole as “polar rings” ($\theta \approx 0$), and those near the equator as “equatorial rings” ($\theta \approx \pi/2$). In this paper, we compute the energy transfers among the rings, and show that the energy transfers are dominant near the plane perpendicular to the external magnetic field when the external field is large. We also compute other quantities like energy flux, conical energy flux, and ring dissipation rates. These results provide newer insights, and they are consistent with earlier results on two-dimensionalization of the liquid metal MHD flows.^{6,7,15} Note however that our work differs from those of Favier *et al.*^{7,13}. We explicitly compute the energy transfers, in contrast to Favier *et al.*^{7,13} who focus on energy spectra of poloidal and toroidal components, anisotropy of the flow, as well non-linear transfer spectrum.

The paper is organized as follows: In Sec. II, we present the formalism of ring-to-ring energy transfers, conical energy flux, and parallel and perpendicular energy fluxes. Section III contains the details of our numerical simulations. We present the results of our numerical computations in Sec. IV, and summarize the results in Sec. V.

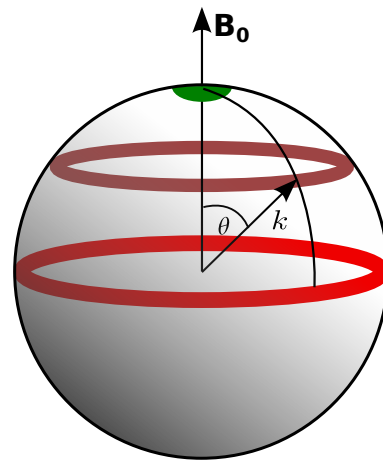


FIG. 1. Ring decomposition of the Fourier space.^{15,24}

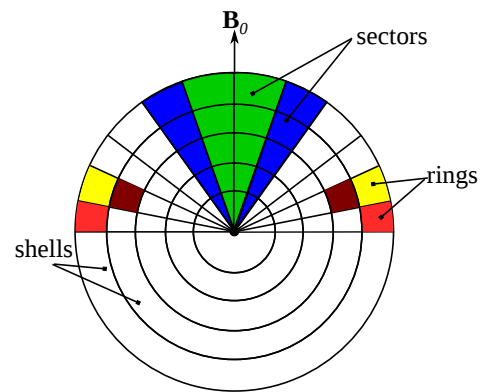


FIG. 2. A cross-sectional view of wavenumber shells, sectors, and rings.

II. THEORETICAL FRAMEWORK

A. Governing equations

The governing equations for liquid metal MHD under quasi-static approximation are:^{1,2}

$$\begin{aligned} \frac{\partial \mathbf{u}}{\partial t} + (\mathbf{u} \cdot \nabla) \mathbf{u} &= -\nabla(p/\rho) - \frac{\sigma B_0^2}{\rho} \frac{1}{\nabla^2} \frac{\partial^2 \mathbf{u}}{\partial z^2} \\ &\quad + \nu \nabla^2 \mathbf{u} + \mathbf{f}, \end{aligned} \quad (1)$$

$$\nabla \cdot \mathbf{u} = 0, \quad (2)$$

where \mathbf{u} is the velocity field, $\mathbf{B}_0 = B_0 \hat{z}$ is the constant external magnetic field, p is the pressure, ρ , ν , σ are the density, kinematic viscosity, conductivity of the fluid, respectively, and \mathbf{f} is the forcing. We also assume that the flow is incompressible, i.e., the density of the fluid is constant.

The above equations are nondimensionalized using the characteristic velocity U_0 as the velocity scale, the box dimension L_0 as the length scale, and L_0/U_0 as the time

scale. As a result, the non-dimensional equations are

$$\frac{\partial \mathbf{U}}{\partial T} + (\mathbf{U} \cdot \nabla') \mathbf{U} = -\nabla' P - B_0'^2 \frac{1}{\nabla'^2} \frac{\partial^2 \mathbf{U}}{\partial Z'^2} + \nu' \nabla'^2 \mathbf{U} + \mathbf{f}', \quad (3)$$

$$\nabla' \cdot \mathbf{U} = 0, \quad (4)$$

where non-dimensional variables are $\mathbf{U} = \mathbf{u}/U_0$, $\nabla' = L_0 \nabla$, $T = t(U_0/L_0)$, $B_0'^2 = \sigma B_0^2 L_0 / (\rho U_0)$ and $\nu' = \nu / (U_0 L_0)$.

In quasi-static MHD turbulence, there is an interplay between the Joule dissipation, viscous dissipation, and the non-linear energy transfers at various scales. It is convenient to analyze the aforementioned processes in the wavenumber or the Fourier space. The non-dimensional equations in the spectral space^{5,6,25} are

$$\frac{\partial \hat{U}_i(\mathbf{k})}{\partial T} = -ik_j \sum \hat{U}_j(\mathbf{q}) \hat{U}_i(\mathbf{k} - \mathbf{q}) - ik_i \hat{P}(\mathbf{k}) - B_0'^2 \cos^2(\theta) \hat{U}_i(\mathbf{k}) - \nu' k^2 \hat{U}_i(\mathbf{k}) + \hat{f}'_i(\mathbf{k}), \quad (5)$$

$$k_i \hat{U}_i(\mathbf{k}) = 0, \quad (6)$$

where $\hat{U}_i(\mathbf{k})$ and $\hat{f}'_i(\mathbf{k})$ are the Fourier transforms of the velocity and force fields respectively, and θ is the angle between wavenumber vector \mathbf{k} and the external magnetic field \mathbf{B}_0 .

The Reynolds number, which is the ratio of the nonlinear term to the viscous term, is a measure of nonlinearity in the flow. The interaction parameter, which is the ratio of the Lorentz force and the nonlinear term, quantifies the strength of the Lorentz force. The interaction parameter N is defined as

$$N = \frac{B_0'^2 L}{U'}, \quad (7)$$

where U' is the root mean square (rms) of the velocity defined^{11,26} as

$$\frac{3}{2} U'^2 = E = \int_0^\infty E(k) dk, \quad (8)$$

and L is the the non-dimensional integral length scale defined as

$$L = \frac{\pi}{2U'^2} \int_0^{k_{max}} \frac{E(k)}{k} dk, \quad (9)$$

where $E(k)$ is the one-dimensional energy spectrum. The energy equation corresponding to Eq. (5) is

$$\frac{\partial E(\mathbf{k})}{\partial T} = T(\mathbf{k}) - 2B_0'^2 \cos^2(\theta) E(\mathbf{k}) - 2\nu' k^2 E(\mathbf{k}) + F(\mathbf{k}), \quad (10)$$

where $E(\mathbf{k}) = |\hat{\mathbf{U}}(\mathbf{k})|^2/2$, $F(\mathbf{k})$ is energy supply rate due to external forcing \mathbf{f} , and $T(\mathbf{k})$ is the net nonlinear energy transfer rate to a mode \mathbf{k} . The energy equation contains two dissipative terms: the Joule dissipation rate

$$\epsilon_J(\mathbf{k}) = 2B_0'^2 \cos^2(\theta) E(\mathbf{k}), \quad (11)$$

and viscous dissipation rate

$$\epsilon_\nu(\mathbf{k}) = 2\nu' k^2 E(\mathbf{k}). \quad (12)$$

B. Shell-to-shell and ring-to-ring energy transfers, and conical energy flux

We can study the energy transfers in the Fourier space in detail using the ‘‘mode-to-mode’’ energy transfer proposed by Dar *et al.*²² and Verma.²³ For a triad $(\mathbf{k}, \mathbf{p}, \mathbf{q})$,

$$S(\mathbf{k}|\mathbf{p}|\mathbf{q}) = \Im\{[\mathbf{k} \cdot \hat{\mathbf{U}}(\mathbf{q})][\hat{\mathbf{U}}^*(\mathbf{k}) \cdot \hat{\mathbf{U}}(\mathbf{p})]\}, \quad (13)$$

is the mode-to-mode energy transfer rate from the mode \mathbf{p} to the mode \mathbf{k} with the mode \mathbf{q} acting as a mediator.^{22,23} Here, \Im and $*$ represent imaginary part and complex conjugate of a complex number, respectively. Note that $\mathbf{k} = \mathbf{p} + \mathbf{q}$.

The shell-to-shell energy transfer rate from all the modes in m^{th} shell to the modes in n^{th} shell is defined as

$$T_n^m = \sum_{\mathbf{k} \in n} \sum_{\mathbf{p} \in m} S(\mathbf{k}|\mathbf{p}|\mathbf{q}). \quad (14)$$

The shell-to-shell energy transfer provides an average energy transfer over all angles. To diagnose the angular dependence of energy transfer, we divide the wavenumber shells into rings as shown in Fig. 1. A ring is an intersection of a shell and a sector (see Fig. 2), hence it is characterized by (m, α) , where m denotes the shell index, and α represents the sector index. The ring-to-ring energy transfer rate from the ring (m, α) to the ring (n, β) is²⁴

$$T_{(n,\beta)}^{(m,\alpha)} = \sum_{\mathbf{k} \in (n,\beta)} \sum_{\mathbf{p} \in (m,\alpha)} S(\mathbf{k}|\mathbf{p}|\mathbf{q}). \quad (15)$$

The ring-to-ring energy transfers are normalized using $A_i = |\cos(\theta_i) - \cos(\theta_{i+1})|$ to compensate for the uneven distribution of modes in the rings.²⁴ The rings closer to the equator have more Fourier modes than those near the poles. Hence we define a normalized ring energy transfer function as

$$\bar{T}_{(n,\beta)}^{(m,\alpha)} = \frac{1}{A_\alpha A_\beta} T_{(n,\beta)}^{(m,\alpha)}. \quad (16)$$

The properties of the ring-to-ring transfers are listed by Teaca *et al.*²⁴ For example, the energy transfer rates between rings within a shell vanish for isotropic flows. In this paper, we will adopt Teaca *et al.*'s²⁴ procedure for these computations.

To further quantify the anisotropic energy transfers we compute another quantity called the conical energy flux $\Pi(\theta)$. Consider a cone of half-angle θ shown in Fig. 3. The conical energy flux $\Pi(\theta)$ is defined as the total energy transfer from the modes inside the cone to the modes outside the cone (from region G to region R of Fig. 3):

$$\Pi(\theta) = \sum_{\mathbf{k} \in R} \sum_{\mathbf{p} \in G} S(\mathbf{k}|\mathbf{p}|\mathbf{q}). \quad (17)$$

We also calculate the energy E_α in the sector α as

$$E_\alpha = \sum_{\mathbf{k} \in \alpha} \frac{1}{2} |\hat{\mathbf{U}}(\mathbf{k})|^2. \quad (18)$$

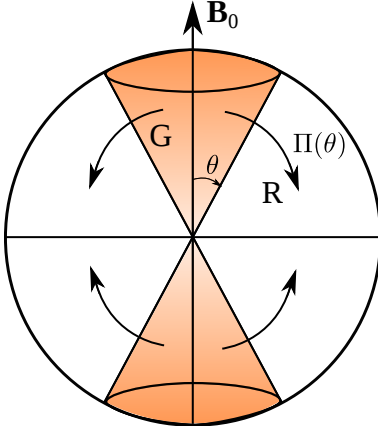


FIG. 3. Conical energy flux $\Pi(\theta)$ is the rate of energy transfer from the modes inside a cone of half-angle θ to the modes outside the cone (see Sec. IV C).

For a strong external field, the energy is concentrated near the equatorial regions (perpendicular to the mean magnetic field). The energies in the equatorial and non-equatorial sectors are given by

$$E_{\text{eq}} = \sum_{\mathbf{k} \in \alpha_{\text{eq}}} \frac{1}{2} |\hat{\mathbf{U}}(\mathbf{k})|^2, \quad (19)$$

$$E_{\text{non-eq}} = \sum_{\mathbf{k} \notin \alpha_{\text{eq}}} \frac{1}{2} |\hat{\mathbf{U}}(\mathbf{k})|^2, \quad (20)$$

respectively. Here α_{eq} represents the equatorial sector spanning angles $[\frac{7\pi}{15}, \frac{\pi}{2}]$.

C. Energy exchange between perpendicular and parallel velocity components

Another interesting feature of anisotropic flows is the energy exchange between the perpendicular and parallel components of the velocity field ($U_{\parallel} = \mathbf{U} \cdot \hat{z}$ and $\mathbf{U}_{\perp} = \mathbf{U} - U_{\parallel} \hat{z}$ respectively). Here, we compute these transfers using the energy fluxes of the parallel and perpendicular components of the velocity field (see Appendix A). In brief, the energy equations for the perpendicular and parallel components of the velocity field are

$$\frac{\partial E_{\perp}(\mathbf{k})}{\partial t} = \sum_{\mathbf{k}=\mathbf{p}+\mathbf{q}} S_{\perp}(\mathbf{k}|\mathbf{p}|\mathbf{q}) - 2B_0'^2 \cos^2(\theta) E_{\perp}(\mathbf{k}) + P_{\perp}(\mathbf{k}) - 2\nu' k^2 E_{\perp}(\mathbf{k}) + \Re\{\hat{\mathbf{f}}'_{\perp}(\mathbf{k}) \cdot \hat{\mathbf{U}}_{\perp}^*(\mathbf{k})\}, \quad (21)$$

$$\frac{\partial E_{\parallel}(\mathbf{k})}{\partial t} = \sum_{\mathbf{k}=\mathbf{p}+\mathbf{q}} S_{\parallel}(\mathbf{k}|\mathbf{p}|\mathbf{q}) - 2B_0'^2 \cos^2(\theta) E_{\parallel}(\mathbf{k}) + P_{\parallel}(\mathbf{k}) - 2\nu' k^2 E_{\parallel}(\mathbf{k}) + \Re\{\hat{f}'_{\parallel}(k) \hat{U}_{\parallel}^*(k)\}, \quad (22)$$

where $E_{\perp}(\mathbf{k}) (= \frac{1}{2} |\hat{\mathbf{U}}_{\perp}(\mathbf{k})|^2)$ and $E_{\parallel}(\mathbf{k}) (= \frac{1}{2} |\hat{U}_{\parallel}(\mathbf{k})|^2)$ are the energies of the perpendicular and parallel com-

ponents of the velocity field, respectively, and

$$S_{\perp}(\mathbf{k}|\mathbf{p}|\mathbf{q}) = \Im\{[\mathbf{k} \cdot \hat{\mathbf{U}}(\mathbf{q})][\hat{\mathbf{U}}_{\perp}^*(\mathbf{k}) \cdot \hat{\mathbf{U}}_{\perp}(\mathbf{p})]\}, \quad (23)$$

$$S_{\parallel}(\mathbf{k}|\mathbf{p}|\mathbf{q}) = \Im\{[\mathbf{k} \cdot \hat{\mathbf{U}}(\mathbf{q})][\hat{U}_{\parallel}^*(\mathbf{k}) \hat{U}_{\parallel}(\mathbf{p})]\}, \quad (24)$$

$$P_{\perp}(\mathbf{k}) = \Im\{[\mathbf{k}_{\perp} \cdot \hat{\mathbf{U}}_{\perp}^*(\mathbf{k})] \hat{P}(\mathbf{k})\}, \quad (25)$$

$$P_{\parallel}(\mathbf{k}) = \Im\{[k_{\parallel} \hat{U}_{\parallel}^*(\mathbf{k})] \hat{P}(\mathbf{k})\}, \quad (26)$$

and \Re , \Im , $*$ represent the real and imaginary parts, and the complex conjugate a complex number, respectively. In the above equations we have replaced \mathbf{k}' and $\hat{\mathbf{U}}(\mathbf{k}')$ in the equations of Appendix A with $-\mathbf{k}$ and $\hat{\mathbf{U}}^*(\mathbf{k})$ respectively. Also note that Eqs. (25,26) and the condition $\mathbf{k} \cdot \hat{\mathbf{U}}(\mathbf{k}) = 0$ imply that

$$P_{\perp}(\mathbf{k}) = -P_{\parallel}(\mathbf{k}). \quad (27)$$

We interpret the above result as following. The energy gained by the perpendicular component $\hat{\mathbf{U}}_{\perp}^*(\mathbf{k})$ via pressure is equal and opposite to the energy lost by the parallel component via pressure is given by Eq. (25). Thus pressure facilitates energy transfers between the parallel and perpendicular components of the velocity field. Note that there is no direct energy transfer between $\hat{\mathbf{U}}_{\perp}$ and \hat{U}_{\parallel} .

The energy flux $\Pi_{\perp}(k_0)$ for the perpendicular component of the velocity field for a wavenumber sphere of radius k_0 is defined as the net energy transfer from the modes $\mathbf{U}_{\perp}(\mathbf{p})$ residing inside the sphere to the modes $\mathbf{U}_{\perp}(\mathbf{k})$ outside the sphere, i.e.,

$$\Pi_{\perp}(k_0) = \sum_{|\mathbf{k}| \geq k_0} \sum_{|\mathbf{p}| < k_0} S_{\perp}(\mathbf{k}|\mathbf{p}|\mathbf{q}). \quad (28)$$

A similar formula for the flux of the parallel velocity component, $\Pi_{\parallel}(k_0)$, is

$$\Pi_{\parallel}(k_0) = \sum_{|\mathbf{k}| \geq k_0} \sum_{|\mathbf{p}| < k_0} S_{\parallel}(\mathbf{k}|\mathbf{p}|\mathbf{q}). \quad (29)$$

We will compute these quantities using our simulation data.

In the following section, we describe the details of simulation method employed for the present study.

III. DETAILS OF NUMERICAL SIMULATIONS

We use pseudo-spectral code *Tarang*²⁷ to solve the non-dimensional quasi-static MHD equations (Eqs. (3) and (4)) in a cubical box on a 256^3 grid. Periodic boundary condition is applied in all the three directions. We use fourth-order Runge-Kutta method for time-stepping, Courant-Friedrichs-Lewy (CFL) condition for calculating time-step (Δt), and the 3/2 rule for dealiasing.^{28,29} We start our simulation for $N = 0$ using a model energy spectrum³⁰ as an initial condition:

$$E(k) = C \epsilon^{2/3} k^{-5/3} f_L(kL) f_{\eta}(k\eta), \quad (30)$$

with the Kolmogorov constant $C = 1.5$, and the energy supply rate $\epsilon = 1.0$. f_L, f_η are defined as

$$f_L(kL) = \left(\frac{kL}{[(kL)^2 + c_L]^{1/2}} \right)^{5/3+p_0}, \quad (31)$$

$$f_\eta(k\eta) = \exp(-\beta k\eta), \quad (32)$$

where $c_L = 1.5$, $p_0 = 2$ and $\beta = 5.2$. The initial phases of the velocity Fourier modes are randomly generated.

In order to achieve a steady-state, the velocity field is randomly forced using a scheme similar to that followed by Burattini *et al.*,¹¹ Vorobev *et al.*,²⁶ and Carati *et al.*,³¹ which is,

$$\hat{\mathbf{f}}'(\mathbf{k}) = \gamma(\mathbf{k})\hat{\mathbf{U}}(\mathbf{k}), \quad (33)$$

$$\gamma(\mathbf{k}) = \frac{\epsilon_{in}}{n_f[\hat{\mathbf{U}}(\mathbf{k}) \cdot \hat{\mathbf{U}}^*(\mathbf{k})]}, \quad (34)$$

where n_f is total number of modes inside the forcing wavenumber band. We choose the energy input rate $\epsilon_{in} = 0.1$, and the forcing band as $1 \leq |\mathbf{k}| \leq 3$ for the shell-to-shell, ring-to-ring, and conical flux studies. However, we choose the forcing band as $8 \leq |\mathbf{k}| \leq 9$ for the computation of the energy fluxes of the parallel and perpendicular components of the velocity field

TABLE I. Details of simulations: the constant external magnetic field B'_0 , forcing band k_f , the interaction parameter N computed at steady state, the interaction parameter N_0 computed at the instant when external magnetic field is applied, rms velocity U' , eddy turnover time τ , and time averaged $k_{\max}\eta$.

B'_0	k_f	N	N_0	U'	τ	$k_{\max}\eta$
2.29	[1-3]	1.7	1.0	0.39	0.32	2.4
3.60	[1-3]	5.5	2.5	0.35	0.43	2.8
5.15	[1-3]	11	5.0	0.39	0.39	2.9
6.26	[1-3]	14	7.5	0.45	0.37	2.9
7.28	[1-3]	18	10.0	0.51	0.33	2.8
10.23	[1-3]	27	20.0	0.65	0.26	2.6
25.1	[1-3]	130	–	0.86	0.21	2.4
32.6	[1-3]	220	–	0.87	0.21	2.4
19.6	[8-9]	100	30	0.64	0.26	2.1

We choose a fixed value for the non-dimensional viscosity ν' as 0.00036, and vary the non-dimensional external magnetic field B'_0 to simulate N 's ranging from 1.7 to 220. The final state of $N = 0$ is used as the initial condition for $N = 1.7, 5.5, 11, 14, 18$ and 27, and all the simulations are carried out till a new statistically steady-state is reached. However, for high interaction parameter, i.e., $N = 130$ and 220 we have used the final state of $N = 27$ as the initial condition. The interaction parameter N is calculated using the values of U' and L of the steady state.¹⁵

For all our simulations, the grid resolution is chosen such that $k_{\max}\eta > 1.4$, where k_{\max} is the largest wavenumber of the simulation, and η is the Kolmogorov length scale. Hence, the smallest length scale of the flow

is larger than the grid size.^{7,32} Thus our simulations are fully resolved. We refer to Reddy and Verma¹⁵ for the details on grid independence tests.

We compute the energy transfer rates using the simulation data and the formulas defined in Sec. II. For the shell-to-shell energy transfers, we divide the Fourier space into 20 spherical shells. The chosen wavenumber shell radii are: 4.0, 8.0, 8.9, 9.9, 10.9, 12.2, 13.5, 14.9, 16.6, 18.4, 20.5, 22.7, 25.2, 28.0, 31.1, 34.5, 38.3, 42.5 and 85.0. For the ring-to-ring and the conical flux transfers, the aforementioned shells are further divided into rings. In our simulation, we work with the modes with $k_z \geq 0$ or $0 \leq \theta \leq \pi/2$ by exploiting the reality condition. We divide the Fourier space into 15 equi-spaced sectors for $0 \leq \theta \leq \pi/2$. The range of angles for the i^{th} sector is $[\frac{(i-1)\pi/2}{15}, \frac{i\pi/2}{15})$ with $i = 1 : 15$. The results of our simulation data are presented in the following section.

IV. NUMERICAL RESULTS

We compute various energy transfer rates for $N = 1.7, 5.5, 11, 14, 18, 27, 130$ and 220. A detailed description of each transfer are described in the following subsections.

A. Shell-to-shell energy transfers

In Fig. 4 we present the shell-to-shell energy transfer rates for $N = 1.7, 11, 18$, and 130. We observe that n^{th} shell gives energy to $(n+l)^{\text{th}}$ shells ($l > 0$), and it receives energy from $(n-l)^{\text{th}}$ shells. Thus, the shell-to-shell energy transfer for quasi-static MHD is forward. We also observe that the maximum energy transfer is to the nearest neighbor, i.e., the n^{th} shell gives maximum positive energy transfer to $(n+1)^{\text{th}}$ shell, and maximum negative energy to $(n-1)^{\text{th}}$ shell. Hence, the shell-to-shell energy transfer is also local. Our results are consistent with those results of Burattini *et al.*¹¹.

B. Ring-to-ring energy transfers

The angular dependence of the energy transfers can be computed using the ring-to-ring transfers. In Figs. 5, 6 and 7 we illustrate the normalized ring-to-ring energy transfers $\bar{T}_{(n,\beta)}^{(m,\alpha)}$ from the rings of the 9th shell ($m = 9$) to the rings of the shells $n = 9, 10$, and 8, respectively. This analysis has been performed for $N = 1.7, 11, 18$ and 130. In these figures, the vertical axis represents the sector index for the giver ring (α), while the horizontal axis represents the sector index for the receiver ring (β).

First we discuss $\bar{T}_{(9,\beta)}^{(9,\alpha)}$, i.e., the energy transfers among the rings with shell index 9. Figure 5 shows that the energy transfer from ring α to ring $(\alpha - 1)$ is positive ($\bar{T}_{(9,\alpha-1)}^{(9,\alpha)} > 0$), and from ring α to the ring $(\alpha + 1)$ is

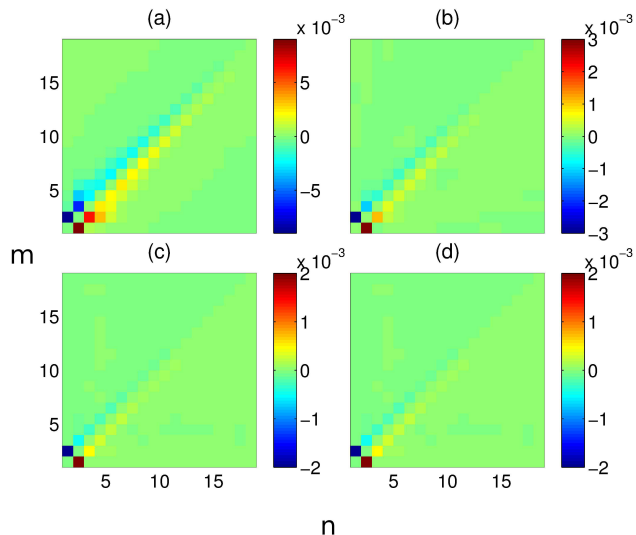


FIG. 4. Forward and local shell-to-shell energy transfer rates for: (a) $N = 1.7$, (b) $N = 11$, (c) $N = 18$ and (d) $N = 130$. m and n are the giver and receiver shells respectively.

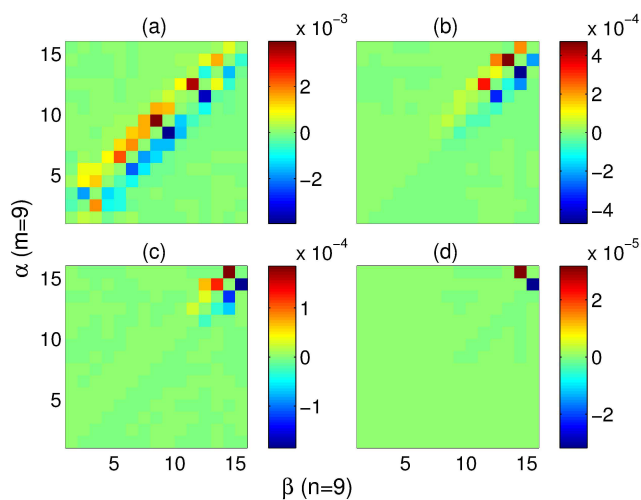


FIG. 5. Ring-to-ring energy transfers $\bar{T}_{(9,\beta)}^{(9,\alpha)}$ among various rings of the 9th shell for: (a) $N = 1.7$, (b) $N = 11$, (c) $N = 18$ and (d) $N = 130$. α and β are the giver and receiver rings respectively. $\bar{T}_{(9,\beta)}^{(9,\alpha)}$ are dominant for the neighboring rings (local). For large N , the energy transfers are dominant near the equator.

negative ($\bar{T}_{(9,\alpha+1)}^{(9,\alpha)} < 0$). Hence, the ring-to-ring energy transfer within a shell is from the equatorial region to the polar region. Among the rings, the most significant energy transfers occur between the neighboring rings, i.e., from a ring with index α to the rings $\alpha \pm 1$. Hence, the energy transfer is local in the angular direction as well. Another important conclusion that can be drawn from the above computation is that for large N ($N = 11, 18, 130$),

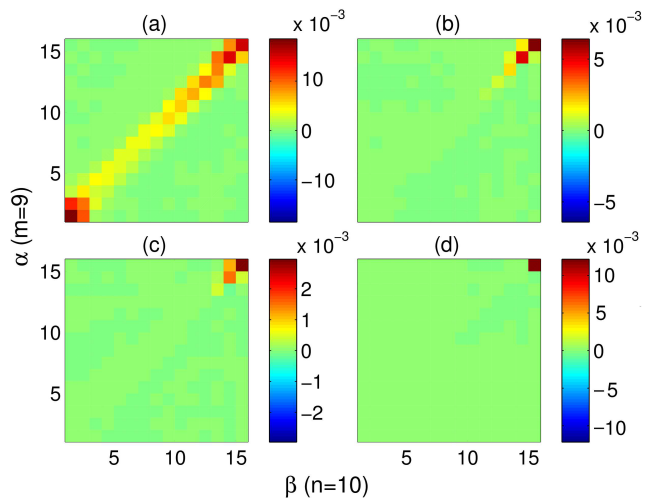


FIG. 6. Local ring-to-ring energy transfers $\bar{T}_{(10,\beta)}^{(9,\alpha)}$ from the rings of the 9th shell and to the rings of the 10th shell for: (a) $N = 1.7$, (b) $N = 11$, (c) $N = 18$ and (d) $N = 130$. Note that $\bar{T}_{(10,\beta)}^{(9,\alpha)} > 0$.

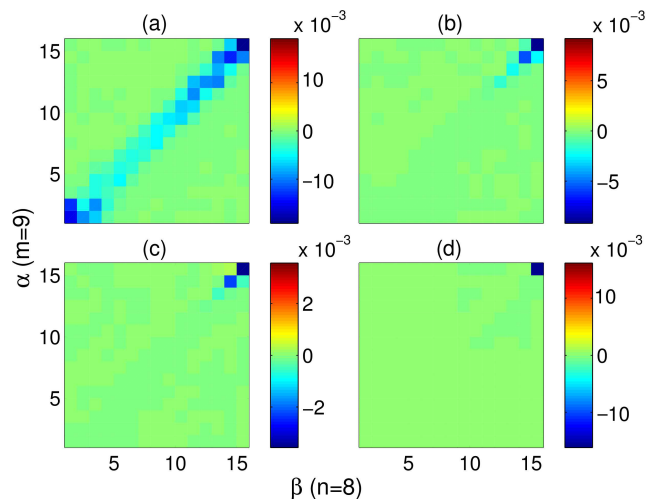


FIG. 7. Local ring-to-ring energy transfers $\bar{T}_{(8,\beta)}^{(9,\alpha)}$ from the rings of the 9th shell and to the rings of the 8th shell for: (a) $N = 1.7$, (b) $N = 11$, (c) $N = 18$ and (d) $N = 130$. Note that $\bar{T}_{(8,\beta)}^{(9,\alpha)} < 0$.

the dominant energy transfer takes place from the equatorial rings to its neighbors (lower θ).

Figure 6 illustrates $\bar{T}_{(10,\beta)}^{(9,\alpha)}$, i.e., energy transfers from the rings in the 9th shell to those in the 10th shell. The figure shows that $\bar{T}_{(10,\beta)}^{(9,\alpha)} > 0$, and they are most dominant for the equatorial rings ($\alpha, \beta \approx 15$). Since $\bar{T}_{(10,\beta)}^{(9,\alpha)}$ dominates for $\alpha = \beta$, we conclude that the energy is transferred dominantly along a sector near the equator. Hence, the energy transfers are forward along the sectors

as well. This feature is reinforced by the $\overline{T}_{(8,\beta)}^{(9,\alpha)}$ illustrated in Fig. 7, where we observe a negative energy being transferred diagonally from the rings of shell 9 to the rings of shell 8. Thus, the ring-to-ring transfers are local and forward. For large N , these transfers tend to be dominant near the equator.

In the next subsection, we will describe conical energy flux.

C. Conical Energy Flux

We can integrate the ring energy transfers over sectors and compute the conical energy flux [see Eq. (17)]. This quantity describes the energy flux leaving a cone in the Fourier space (see Fig. 3). In Fig. 8 we plot the normalized flux $\Pi(\theta)/\max(|\Pi(\theta)|)$. The figure shows that for $N = 1.7$ to 130, the above flux is negative, indicating that the energy is transferred from the modes outside the cone to the modes into the cone. Note that $\Pi(\theta)/\max(|\Pi(\theta)|)$ is monotonic except for $N = 1.7$ (due to relatively weak magnetic field). We also observe that the maximal energy transfer takes place for the cone with a half angle $\theta \approx \pi/2$. Hence, the modes near the equatorial region transfer maximal energy towards smaller θ . This energy gets dissipated by Joule heating, as well as it trickles down to the polar region.

In Fig. 9 we plot the net energy transferred by the cone with the largest half-angle:

$$\Pi_{\text{eq}} = \sum_{\theta_p < \frac{7\pi}{15}} \sum_{\theta_k \geq \frac{7\pi}{15}} S(\mathbf{k}|\mathbf{p}|\mathbf{q}), \quad (35)$$

The quantity $-\Pi_{\text{eq}}$ quantifies the energy transfer from the equatorial region to the modes inside the largest cone. The figure indicates that the $|\Pi_{\text{eq}}|$ decreases very sharply with N , and follows $|\Pi_{\text{eq}}(N)| \propto N^{-1.2}$.

The decrease in $|\Pi_{\text{eq}}|$ can be qualitatively understood using the energy distribution in the Fourier space. In Fig. 10 we plot the total energy and energy contained in the equatorial region. The remaining energy $E_{\text{non-eq}} = E - E_{\text{eq}}$ is also plotted in the figure. We find that $E_{\text{non-eq}}$ decreases sharply with N ($E_{\text{non-eq}} \propto N^{-1.8}$). Since the energy flux is a sum of $E(\mathbf{p})E(\mathbf{q})$, $E(\mathbf{k})E(\mathbf{p})$, and $E(\mathbf{k})E(\mathbf{q})$ apart from some factors (here $\mathbf{k} = \mathbf{p} + \mathbf{q}$)^{21,23}, and the receiver energy spectrum $E_{\text{non-eq}} \propto N^{-1.8}$, it is reasonable that the conical energy flux $|\Pi_{\text{eq}}|$ decreases very sharply. Thus we provide a qualitative explanation for the sharp decline of Π_{eq} with the interaction parameter. This observation also explains why quasi-static MHD is quasi two-dimensional for large N .

D. Energy fluxes of the parallel and perpendicular components

Many experiments^{3,4} and numerical simulations^{6,7,15} indicate that the liquid metal MHD exhibits quasi two-dimensional behavior for large N . To probe the physics

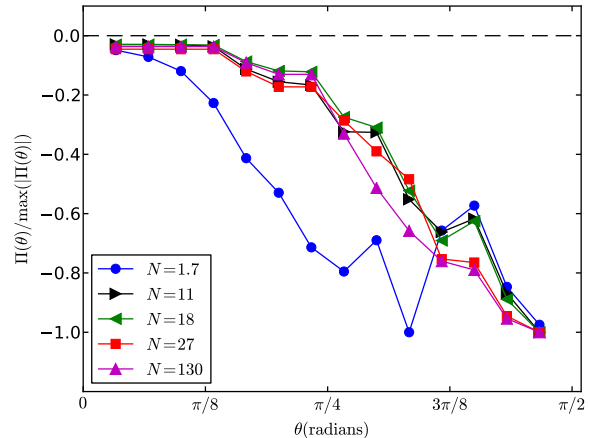


FIG. 8. Normalized conical energy flux $\Pi(\theta)/\max(|\Pi(\theta)|)$ coming out of a cone of half angle θ as a function of θ for various N 's.

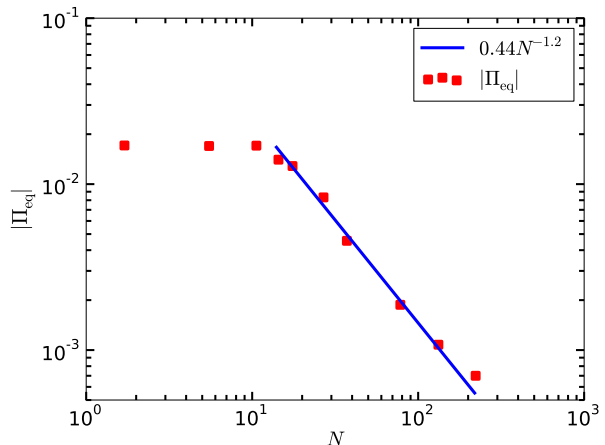


FIG. 9. Plot of $|\Pi_{\text{eq}}|$ coming out of the equatorial sector as a function of N . $\Pi_{\text{eq}} \sim \text{const}$ for small N , but $\Pi_{\text{eq}} \sim N^{-1.2}$ for $N > 10$.

of energy transfers for large N in detail, we perform a numerical simulation for $N = 100$ with forcing applied at intermediate length scales ($8.0 \leq |\mathbf{k}_f| \leq 9.0$) to resolve the inverse and forward cascade regimes. We take the final state of hydrodynamic simulation as an initial condition (see Sec. III) and apply an external magnetic field. The simulation is carried out till a final (quasi-steady) state is reached, which occurs at $t_{\text{final}} \approx 400$.

In Fig. 11 we plot the energy spectrum of the parallel and perpendicular components of the velocity field for $N = 100$. The figure indicates that $E_{\perp} \gg 2E_{\parallel}$ for $k < k_f$, but $E_{\perp} \ll 2E_{\parallel}$ for $k > k_f$. We also observe that $E_{\perp}(k)$ follows $k^{-5/3}$ for $k < k_f$. This feature demonstrates 2D-3C (2D and 3 components) nature of

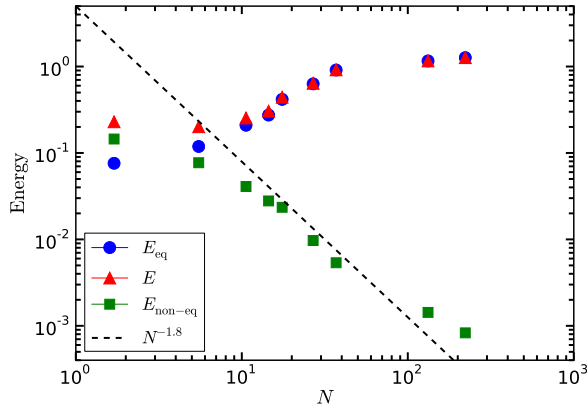


FIG. 10. Plots of E , E_{eq} , $E_{\text{non-eq}}$ vs. N . $E_{\text{non-eq}} \sim N^{-1.8}$ for $N > 10$.

the quasi-static MHD. Our results are consistent with those of Favier *et al.*⁷ To probe the flow physics further, we compute the energy fluxes of the parallel and perpendicular components of the velocity field.

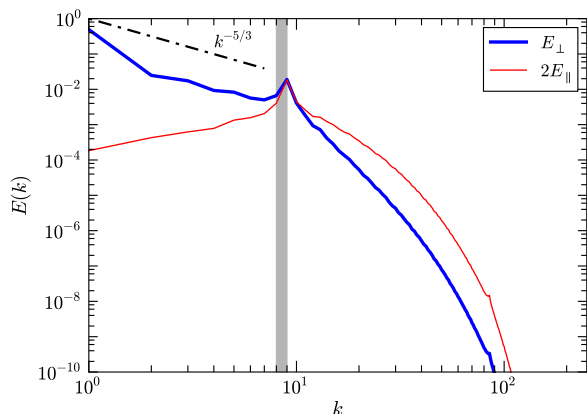


FIG. 11. Plots of $E_{\perp}(k)$ and $2E_{\parallel}(k)$ for $N = 100$. $E_{\perp}(k) > E_{\parallel}(k)$ for $k < k_f$ with $E_{\perp}(k) \sim k^{-5/3}$, but $E_{\perp}(k) < E_{\parallel}(k)$ for $k > k_f$. The shaded region exhibit the forcing band $k_f \in [8, 9]$.

Figure 12 exhibits the energy fluxes for the parallel and perpendicular components of velocity field (Π_{\parallel} and Π_{\perp} respectively). We observe that the $k < k_f$ and $k > k_f$ regions are dominated by Π_{\perp} and Π_{\parallel} fluxes, respectively. A negative energy flux for Π_{\perp} is consistent with the inverse cascade of \mathbf{U}_{\perp} , while $\Pi_{\parallel} > 0$ indicates a forward cascade of U_{\parallel} . Thus, the aforementioned energy flux computations are consistent with the dominance of $E_{\perp}(k)$ for lower wavenumbers, and $E_{\parallel}(k)$ for higher wavenumbers (see Fig. 11). Thus our energy spectrum and flux computations demonstrate that the the quasi-static MHD is two-dimensional but with three components, as proposed

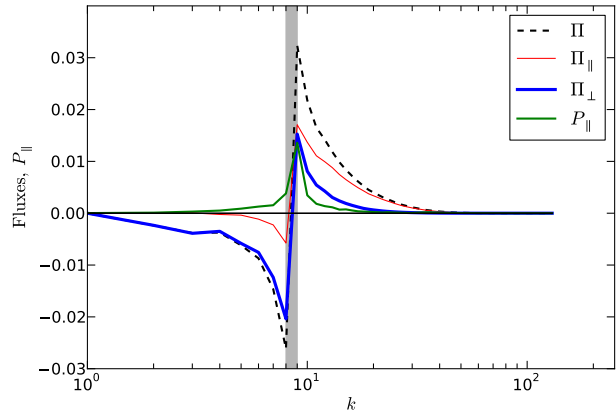


FIG. 12. For $N = 100$, plots of energy flux $\Pi(k)$, $\Pi_{\parallel}(k)$, $\Pi_{\perp}(k)$, and $P_{\parallel}(k)$. $\Pi_{\perp}(k) < 0$ for $k < k_f$ indicating an inverse cascade for \mathbf{U}_{\perp} , while $\Pi_{\parallel}(k) > 0$ for $k > k_f$ indicating a forward cascade for U_{\parallel} . $P_{\parallel}(k) > 0$ for $k > k_f$ indicating an energy transfers from \mathbf{U}_{\perp} to U_{\parallel} via pressure.

by Favier *et al.*⁷

In Fig. 12 we also plot $P_{\parallel}(k)$, which is the energy transferred to $U_{\parallel}(k)$ from $\mathbf{U}_{\perp}(k)$ via pressure. We observe that $P_{\parallel}(k)$ is positive for $k \geq k_f$. Hence $U_{\parallel}(k)$ receives energy from $\mathbf{U}_{\perp}(k)$, consistent with the nature of energy fluxes Π_{\parallel} and Π_{\perp} described above.

E. Dissipation rates

The aforementioned preferential energy transfer from the equatorial region to the polar region can be understood using the distribution of Joule dissipation ϵ_J , which is proportional to $\cos^2 \theta E(\mathbf{k})$ [see Eq. (11)]. Clearly ϵ_J vanishes at the equatorial plane where $\theta = \pi/2$. However, $E(\mathbf{k})$ increases monotonically with θ .^{15,16} As a result, the Joule dissipation ϵ_J peaks at $\theta \approx \pi/2$, not at $\theta = \pi/2$. To maintain a steady state, ϵ_J is balanced by a nonlinear energy transfer from the equatorial region. This is the reason why the energy flows maximally from the equator towards the polar region (see Figs. 5 and 8).

For large N , $E(\mathbf{k})$ is concentrated near the equator. Therefore ϵ_J peaks near $\theta = \pi/2$. As a result, the ring-to-ring energy transfers are localized near the equator, as exhibited in Figs. 5(c,d), 6(c,d), and 7(c,d). These results are consistent with the quasi two-dimensional nature of the flow for large N .^{3,6,7}

Lastly we study the viscous and Joule dissipation rates for a large interaction parameter, here $N = 27$. Since

$$\frac{\epsilon_{\nu}(k, \theta)}{\epsilon_J(k, \theta)} = \frac{2\nu'k^2 E(\mathbf{k})}{2B_0'^2 \cos^2 \theta E(\mathbf{k})} = \frac{2\nu'k^2}{2B_0'^2 \cos^2 \theta}, \quad (36)$$

$\epsilon_J(k, \theta)$ dominates $\epsilon_\nu(k, \theta)$ for

$$k < k_* = B'_0 \cos \theta \sqrt{\frac{1}{\nu}}, \quad (37)$$

and vice-versa. This is expected since the Joule dissipation is active at all wavenumbers, but the viscous dissipation acts strongly only at large wavenumbers. In Fig. 13 we plot $\epsilon_\nu(k, \theta)/\epsilon_J(k, \theta)$ as a function for wavenumber k for various sectors. The mean angles of the chosen sectors are $\theta = 0.05, 0.48, 0.99, 1.41$.

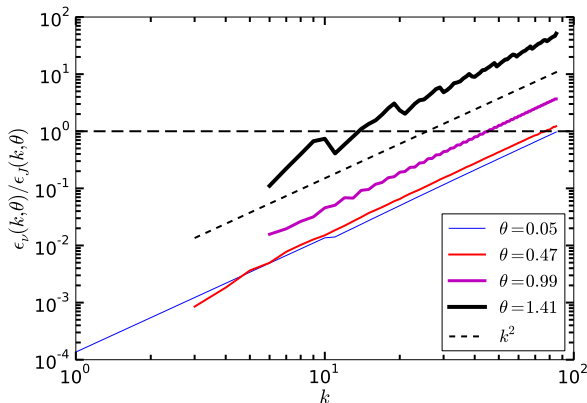


FIG. 13. For $N = 27$, $\epsilon_\nu(k, \theta)/\epsilon_J(k, \theta)$ vs. k for various sectors. $\epsilon_\nu(k, \theta)/\epsilon_J(k, \theta) \sim k^2$.

For a given sector angle θ , the ratio $\epsilon_\nu(k, \theta)/\epsilon_J(k, \theta) \propto k^2$ because the viscous dissipation is proportional to k^2 . Consequently, the Joule dissipation dominates at small wavenumbers, but viscous dissipation takes over at large wavenumbers. For a given wavenumber k , the ratio $\epsilon_\nu(k, \theta)/\epsilon_J(k, \theta) \propto 1/\cos^2 \theta$. As a result, $\epsilon_\nu(k, \theta) \gg \epsilon_J(k, \theta)$ for the equatorial region ($\theta \approx \pi/2$), and vice versa for the polar region ($\theta \approx 0$).

Our results are schematically illustrated in Fig. 14. The perpendicular component of velocity cascades to smaller wavenumbers, while the parallel velocity component cascades to larger wavenumbers, where it gets depleted by the Joule dissipation and via energy cascades to polar region.

V. CONCLUSIONS

Earlier experiments and numerical simulations reveal that the liquid metal MHD under quasi-static approximation exhibit quasi two-dimensional (2-dimension and 3-component, 2D3C) behavior.⁷ In this paper, we have studied energy transfer mechanisms operating in liquid metal MHD, and show them to be consistent with the aforementioned anisotropic energy distribution. Here we have studied the shell-to-shell and ring-to-ring energy transfers, as well as conical flux. We also have studied the energy fluxes of parallel and perpendicular components

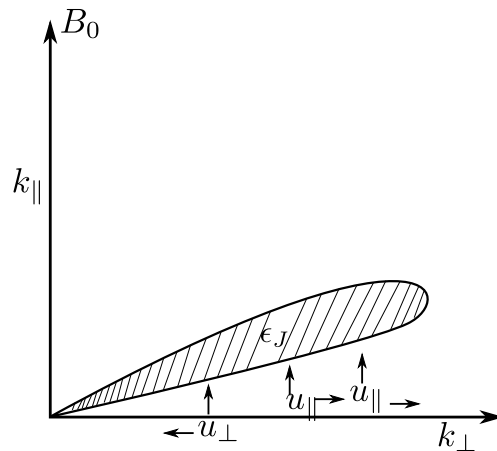


FIG. 14. A schematic illustration of the energy transfers (depicted by arrows) and dissipation rates in quasi-static MHD turbulence for large N . \mathbf{U}_\perp exhibits an inverse cascade, while U_\parallel a forward cascade.

of the velocity field. For most of our runs, our forcing wavenumber band is at small wavenumber regime.

Main results of our paper are:

1. We developed a formalism to compute ring-to-ring and conical energy transfer. We also provided a scheme to compute energy fluxes for the parallel and perpendicular components of the velocity field.
2. The shell-to-shell energy transfers in liquid metal MHD are local and forward, i.e., the shell-to-shell energy transfers are dominantly among the neighboring shells and from lower to higher wavenumber shells, consistent with the results of Burattini *et al.*¹¹
3. The ring-to-ring energy transfers are also local and forward. Within a shell, the ring-to-ring transfers are from higher polar angles to lower polar angles (from the equatorial region to the polar region). For the rings across shells, it is dominantly along the same sector or neighboring sectors.
4. When the flow is forced at an intermediate wavenumber band, for large N we observe an inverse cascade for the perpendicular component of velocity, and forward cascade for the parallel component. This result is consistent with the 2D-3C flow structure observed by Favier *et al.*⁷

In conclusion, the energy transfers in quasi-static MHD provide valuable insights into the physics of the flow.

ACKNOWLEDGMENTS

We thank D. Carati, B. Knaepen, P. Satyamurthy, and D. Biswas for useful discussions. RK thanks

S. V. G. Menon, former Head, Theoretical Physics Division BARC for the encouragement and support. This work was supported by Board of Research in Nuclear Science, Department of Atomic Energy, Govt. of India through research grant 2009/36/81-BRNS. All the simulations were performed on the *HPC system* and *Chaos* cluster of IIT Kanpur.

APPENDIX A: MODE-TO-MODE ENERGY TRANSFERS FOR THE PERPENDICULAR AND PARALLEL COMPONENTS OF THE VELOCITY FIELD

In this appendix, we derive formulas for the energy transfers for the perpendicular and parallel components of the velocity field. We focus on a triad $(\mathbf{k}, \mathbf{p}, \mathbf{q})$ under the limit $\nu = 0$ and $B_0 = 0$. Note that $\mathbf{k}' + \mathbf{p} + \mathbf{q} = 0$, and $\mathbf{k}' = -\mathbf{k}$.

Following Dar *et al.*²² and Verma,²³ we derive the following equations from Eqs. (3,4):

$$\frac{\partial E_{\perp}(\mathbf{k}')}{\partial t} = S_{\perp}(\mathbf{k}'|\mathbf{p}|\mathbf{q}) + S_{\perp}(\mathbf{k}'|\mathbf{q}|\mathbf{p}) + P_{\perp}(\mathbf{k}'), \quad (38)$$

$$\frac{\partial E_{\parallel}(\mathbf{k}')}{\partial t} = S_{\parallel}(\mathbf{k}'|\mathbf{p}|\mathbf{q}) + S_{\parallel}(\mathbf{k}'|\mathbf{q}|\mathbf{p}) + P_{\parallel}(\mathbf{k}'), \quad (39)$$

where $E_{\perp}(\mathbf{k}) = E_{\perp}(\mathbf{k}') = \frac{1}{2}|\hat{\mathbf{U}}_{\perp}(\mathbf{k})|^2$ and $E_{\parallel}(\mathbf{k}) = E_{\parallel}(\mathbf{k}') = \frac{1}{2}|\hat{\mathbf{U}}_{\parallel}(\mathbf{k})|^2$ are the energies of the perpendicular and parallel components of the velocity field, and

$$S_{\perp}(\mathbf{k}'|\mathbf{p}|\mathbf{q}) = -\Im\{\mathbf{k}' \cdot \hat{\mathbf{U}}(\mathbf{q})[\hat{\mathbf{U}}_{\perp}(\mathbf{k}') \cdot \hat{\mathbf{U}}_{\perp}(\mathbf{p})]\}, \quad (40)$$

$$S_{\parallel}(\mathbf{k}'|\mathbf{p}|\mathbf{q}) = -\Im\{\mathbf{k}' \cdot \hat{\mathbf{U}}(\mathbf{q})[\hat{\mathbf{U}}_{\parallel}(\mathbf{k}')\hat{\mathbf{U}}_{\parallel}(\mathbf{p})]\}, \quad (41)$$

$$P_{\perp}(\mathbf{k}') = -\Re\{\mathbf{k}' \cdot \hat{\mathbf{U}}_{\perp}(\mathbf{k}')\hat{P}(\mathbf{k}')\}, \quad (42)$$

$$P_{\parallel}(\mathbf{k}') = -\Re\{[k'_{\parallel}\hat{\mathbf{U}}_{\parallel}(\mathbf{k}')]\hat{P}(\mathbf{k}')\}, \quad (43)$$

and $\Re, \Im, *$ represent the real and imaginary parts, and the complex conjugate of a complex number, respectively. The mode \mathbf{k}' receives energy from modes \mathbf{p} and \mathbf{q} . Similarly we can also derive that

$$\frac{\partial E_{\perp}(\mathbf{p})}{\partial t} = S_{\perp}(\mathbf{p}|\mathbf{q}|\mathbf{k}') + S_{\perp}(\mathbf{p}|\mathbf{k}'|\mathbf{q}) + P_{\perp}(\mathbf{p}), \quad (44)$$

$$\frac{\partial E_{\parallel}(\mathbf{p})}{\partial t} = S_{\parallel}(\mathbf{p}|\mathbf{q}|\mathbf{k}') + S_{\parallel}(\mathbf{p}|\mathbf{k}'|\mathbf{q}) + P_{\parallel}(\mathbf{p}), \quad (45)$$

$$\frac{\partial E_{\perp}(\mathbf{q})}{\partial t} = S_{\perp}(\mathbf{q}|\mathbf{k}'|\mathbf{p}) + S_{\perp}(\mathbf{q}|\mathbf{p}|\mathbf{k}') + P_{\perp}(\mathbf{q}), \quad (46)$$

$$\frac{\partial E_{\parallel}(\mathbf{q})}{\partial t} = S_{\parallel}(\mathbf{q}|\mathbf{k}'|\mathbf{p}) + S_{\parallel}(\mathbf{q}|\mathbf{p}|\mathbf{k}') + P_{\parallel}(\mathbf{q}). \quad (47)$$

Using $\mathbf{k} \cdot \hat{\mathbf{U}}(\mathbf{k}) = 0$, we can show that

$$P_{\perp}(\mathbf{k}') + P_{\parallel}(\mathbf{k}') = 0, \quad (48)$$

$$S_{\perp}(\mathbf{k}'|\mathbf{p}|\mathbf{q}) = -S_{\perp}(\mathbf{p}|\mathbf{k}'|\mathbf{q}), \quad (49)$$

$$S_{\parallel}(\mathbf{k}'|\mathbf{p}|\mathbf{q}) = -S_{\parallel}(\mathbf{p}|\mathbf{k}'|\mathbf{q}). \quad (50)$$

Using the above we can conclude that

$$\frac{\partial E_{\perp}(\mathbf{k}')}{\partial t} + \frac{\partial E_{\perp}(\mathbf{p})}{\partial t} + \frac{\partial E_{\perp}(\mathbf{q})}{\partial t} = P_{\perp}(\mathbf{k}') + P_{\perp}(\mathbf{p}) + P_{\perp}(\mathbf{q}), \quad (51)$$

$$\frac{\partial E_{\perp}(\mathbf{k}')}{\partial t} + \frac{\partial E_{\perp}(\mathbf{p})}{\partial t} + \frac{\partial E_{\perp}(\mathbf{q})}{\partial t} = -\left[\frac{\partial E_{\parallel}(\mathbf{k}')}{\partial t} + \frac{\partial E_{\parallel}(\mathbf{p})}{\partial t} + \frac{\partial E_{\parallel}(\mathbf{q})}{\partial t}\right] \quad (52)$$

Therefore, we can make the following conclusions regarding energy transfers for the parallel and perpendicular components of the velocity field:

1. The total energy (sum of perpendicular and parallel components) for a triad is conserved. However there is an energy transfer between the perpendicular and parallel components via pressure.
2. The perpendicular component $\hat{\mathbf{U}}_{\perp}(\mathbf{k}')$ receives energy by an amount $S_{\perp}(\mathbf{k}'|\mathbf{p}|\mathbf{q})$ from $\hat{\mathbf{U}}_{\perp}(\mathbf{p})$ with $\hat{\mathbf{U}}(\mathbf{q})$ as a mediator. Symmetrically, it also receives energy by an amount $S_{\perp}(\mathbf{k}'|\mathbf{q}|\mathbf{p})$ from the $\hat{\mathbf{U}}_{\perp}(\mathbf{q})$ via $\hat{\mathbf{U}}(\mathbf{p})$. The parallel component $\hat{\mathbf{U}}_{\parallel}(\mathbf{k}')$ receives energy by amounts $S_{\parallel}(\mathbf{k}'|\mathbf{p}|\mathbf{q})$ and $S_{\parallel}(\mathbf{k}'|\mathbf{q}|\mathbf{p})$ from the modes $\hat{\mathbf{U}}_{\parallel}(\mathbf{p})$ and $\hat{\mathbf{U}}_{\parallel}(\mathbf{q})$, respectively (with $\hat{\mathbf{U}}(\mathbf{q})$ and $\hat{\mathbf{U}}(\mathbf{p})$ acting as respective mediators).
3. The perpendicular component $\hat{\mathbf{U}}_{\perp}(\mathbf{k})$ receives energy from the parallel component $\hat{\mathbf{U}}_{\parallel}(\mathbf{p})$ by an amount $P_{\perp}(\mathbf{k}')$, which is equal to $-P_{\parallel}(\mathbf{k}')$. Naturally, the parallel component $\hat{\mathbf{U}}_{\parallel}(\mathbf{k}')$ loses energy by the same amount. Hence, the energy transfer between the parallel and perpendicular components occur via pressure.

- ¹P. H. Roberts, *An Introduction to Magnetohydrodynamics* (Elsevier, New York, 1967).
- ²B. Knaepen and R. Moreau, *Ann. Rev. Fluid Mech.* **40**, 25 (2008).
- ³A. Alemany, R. Moreau, P. L. Sulem, and U. Frisch, *J. Méc.* **18**, 277 (1979).
- ⁴Y. Kolesnikov and A. Tsinober, *Fluid Dynamics* **9**, 621 (1974).
- ⁵U. Schumann, *J. Fluid Mech.* **74**, 31 (1976).
- ⁶O. Zikanov and A. Thess, *J. Fluid Mech.* **358**, 299 (1998).
- ⁷B. Favier, F. S. Godeferd, C. Cambon, and A. Delache, *Phys. Fluids* **22**, 075104 (2010).
- ⁸H. Branover, A. Eidelmann, M. Nagorny, and M. Kireev, *Progress in Turbulence Research* **162**, 64 (1994).
- ⁹S. Eckert, G. Gerbeth, W. Witke, and H. Langenbrunner, *International Journal of Heat and Fluid Flow* **22**, 358 (2001).
- ¹⁰H. K. Moffatt, *J. Fluid Mech.* **28**, 571 (1967).
- ¹¹P. Burattini, M. Kinet, D. Carati, and B. Knaepen, *Physica D* **237**, 2062 (2008).
- ¹²P. Burattini, M. Kinet, D. Carati, and B. Knaepen, *Phys. Fluids* **20**, 065110 (2008).
- ¹³B. Favier, F. S. Godeferd, C. Cambon, A. Delache, and W. J. T. Bos, *J. Fluid Mech.* **681**, 434 (2011).
- ¹⁴D. Montgomery and L. Turner, *Phys. Fluids* **25**, 345 (1982).
- ¹⁵K. S. Reddy and M. K. Verma, *Phys. Fluids* **26**, 025109 (2014).
- ¹⁶A. Pothérat and V. Dymkou, *J. Fluid Mech.* **655**, 174 (2010).

- ¹⁷T. Boeck, D. Krasnov, A. Thess, and O. Zikanov, *Phys. Rev. Lett.* **101**, 244501 (2008).
- ¹⁸R. Klein and A. Pothérat, *Phys. Rev. Lett.* **104**, 034502 (2010).
- ¹⁹A. Pothérat, *EPL* **98**, 64003 (2012).
- ²⁰A. Pothérat, *Magnetohydrodynamics* **48**, 13 (2012).
- ²¹M. Lesieur, *Turbulence in Fluids* (Kluwer Academic, Dordrecht, 1990).
- ²²G. Dar, M. Verma, and V. Eswaran, *Physica D* **157**, 207 (2001).
- ²³M. K. Verma, *Phys. Rep.* **401**, 229 (2004).
- ²⁴B. Teaca, M. K. Verma, B. Knaepen, and D. Carati, *Phys. Rev. E* **79**, 046312 (2009).
- ²⁵B. Knaepen, S. Kassinos, and D. Carati, *J. Fluid Mech.* **513**, 199 (2004).
- ²⁶A. Vorobev, O. Zikanov, P. A. Davidson, and B. Knaepen, *Phys. Fluids* **17**, 125105 (2005).
- ²⁷M. K. Verma, A. Chatterjee, K. S. Reddy, R. K. Yadav, S. Paul, M. Chandra, and R. Samtaney, *Pramana* **81**, 617 (2013).
- ²⁸C. Canuto, M. Y. Hussaini, A. Quarteroni, and T. A. Zhang, *Spectral Methods in Fluid Turbulence* (Springer-Verlag, Berlin, 1998).
- ²⁹J. P. Boyd, *Chebyshev and Fourier Spectral Methods* (Dover Publishers, New York, 2001).
- ³⁰S. B. Pope, *Turbulent Flows* (Cambridge University Press, Cambridge, UK, 2000).
- ³¹D. Carati, S. Ghosal, and P. Moin, *Phys. Fluids* **7**, 606 (1995).
- ³²J. Jiménez, A. A. Wray, P. G. Saffman, and R. S. Rogallo, *J. of Fluid Mech.* **255**, 65 (1993).